Supporting Information

Otterstrom et al. 10.1073/pnas.1411755111

SI Materials and Methods

Microfluidic Flow Cell and Glass Cleaning. Experiments were performed in microfluidic channels formed using either double-sided tape sandwiched between a quartz top and coverslip bottom as described previously (1), or multichannel polydimethylsiloxane (PDMS) chips. PDMS (Slygard 184; Dow Corning)-based multichannel microfluidic chips were formed by standard PDMS cast-molding techniques (2, 3). Each chip housed five microfluidic channels having inner dimensions 0.5 (width) × 0.2 (height) × 10 (length) mm^3 and separated by 0.5 mm. PDMS chips were nonpermanently adhered to the surface of the cleaned glass microscope coverslips (no. 1 thickness; VWR) and housed in a home-built microscope adapter. Inlet and outlet polyethylene tubing (PE20 and PE60, respectively; Intramedic) was coupled to each microfluidic channel to allow for rapid buffer exchange via connection to a syringe pump (NE-1000; New Era Pump Systems, Inc.). All chips and flow channels were used only once.

Virus and IgG/Fab Labeling. Influenza A strains PR/8/34 (H1N1) and A/Aichi/2/68 (X-31, H3N2) propagated in specific pathogen-free eggs were purchased from Charles River and used without further purification. Stock samples were certified by the manufacturer to have 2 mg total viral protein per milliliter. EM confirmed that the viruses used were monodisperse, spherical particles of uniform size (Fig. S6), the latter being due to the method of virus propagation. Labeling was performed by diluting virus stocks 1:3 into HNE buffer (5.0 mM Hepes, 140 mM NaCl, 0.2 mM EDTA, pH 7.4), then adding a 0.5% volume equivalent of octadecyl rhodamine B lipophilic dye (R18; Invitrogen, Inc.) in DMSO to a final dye concentration of 1 µM. The virus–dye mixture was placed on a rotating microtube mixer (Cole-Parmer) for 3 h. Unincorporated dye was removed using a PD-10 desalting column (GE Healthcare), causing ~10-fold virus dilution. Fractions of 200 µL were collected and checked for labeled virus using the microscope setup. The three to four fractions with the highest particle count were pooled into a single volume, aliquoted, frozen using liquid nitrogen, and stored at −80 °C until use. Labeled viruses were confirmed to be infectious (4).

IgG and Fab Production. Human IgG1 antibodies CR6261 and CR8020, were constructed by cloning the heavy and light chain variable regions into a single expression vector containing the IgG1 constant regions. HEK293-F cells were transfected with the IgG expression constructs and the expressed antibodies were purified from serum-free culture supernatants using protein A chromatography (HiTrap; GE Healthcare) followed by a desalting step (HiPrep 26/10; GE Healthcare). The Fab fragments were obtained by IdeS digestion of the purified IgG, followed by protein G purification (GE Healthcare), cation exchange (MonoS; GE Healthcare), and gel filtration (Superdex200; GE Healthcare).

IgG/Fab Labeling and Degree of Labeling Determination. HA-specific antibodies CR6261 and CR8020 were fluorescently labeled with Alexa Fluor 488 (AF488; Molecular Probes) according to manufacturers' guidance. In brief, IgG/Fab fragments were added to AF488 dye in sodium bicarbonate buffer. The solutions were mixed at moderate speed on a Ferris wheel mixer for 2 h and protected from light. Free dye was removed from the sample using a PD10 desalting column (GE Healthcare). AF488-labeled IgG/Fab were eluted into 20 mM sodium acetate, 75 mM NaCl, 5% (vol/vol) sucrose, pH 5.5.

The number of AF488 molecules bound to the IgG/Fab molecules was determined using photobleaching analysis and MALDI mass spectrometry. The degree of labeling was taken as an average of these two results and the percentage of labeled IgG/Fab molecules visualized was estimated from a Poisson calculation (Table S1).

Photobleaching measurements were performed by adsorbing labeled IgG/Fab molecules to a clean glass surface and illuminating with ~5 W/cm^2 488-nm laser power to observe individual photobleaching steps. Distributions of the final bleaching height were extracted and well fit by Gaussian distributions. The initial fluorescence intensity of visualized molecules was divided by the mean intensity identified by Gaussian fitting to obtain the distributions for the number of fluorophores bound to each IgG/Fab (Fig. S3 A, i and B, i). These distributions for IgG were well fit by Poisson distributions to determine the expected number of covalently linked Alexa-488 molecules. The distributions for Fab were reasonably well fit by Poisson distributions, but showed higher than expected population densities at a lower number of linked Alexa-488 molecules, indicating that not all available N-terminal amino groups are equally accessible for labeling.

MALDI mass spectra at mass-to-charge ratios of one ($m/z = 1$) and two ($m/z = 2$) were obtained for unlabeled and Alexa-488–labeled IgG/Fab using sinapinic acid as the matrix. The peak value in the mass spectra of the unlabeled IgG/Fab was subtracted from the mass spectra of the labeled molecules. The shifted mass spectra of the labeled molecules was then divided by the mass of individual Alexa-488 molecules, determined to be 515 Da using molecular structures provided by the manufacturer, to scale the mass values in terms of numbers of covalently linked Alexa-488 molecules (Fig. S3). The resulting spectra were well fit by Poisson distributions to identify the expected number of Alexa-488 per IgG/Fab (Fig. S3 A, ii and B, ii).

Proteoliposome Preparation. Proteoliposomes were composed of a $0.8{:}0.2{:}2.5{\times}10^{-5}$ ratio of molar fractions of DOPC:CH:biotin-DHPE [respectively 1,2-dioleoyl-sn-glycero-3-phosphocholine and Cholesterol (Avanti Polar Lipids); N-((6-(biotinoyl)amino) hexanoyl)-1,2-dihexadecanoyl-sn-glycero-3-phosphoethanolamine triethylammonium salt (Invitrogen)] mixed in chloroform solutions, dried under argon, and then desiccated for 2 h. Dried lipids were suspended in HNE buffer at 5 mg/mL, freeze–thawed five times, then extruded using 0.2 µm-pore size polycarbonate filters (miniextruder; Avanti). Liposomes were solubilized by Triton X-100 (molecular biology grade; VWR International) to a final concentration of 0.5% and incubated at 37 °C for 15 min, then on ice for 15 min. The GYPA (Abnova; full-length recombinant protein with a GST tag) was added to solubilized lipids at a lipid:protein molar ratio of ~1:40,000 and mixed at 4 °C for 30 min. Bio-Beads (SM-2 absorbent; Bio-Rad Laboratories, Inc.) removed the Triton-X detergent through two subsequent 2-h incubations at 4 °C with constant rocking, using 200 mg Bio-Beads per 300 µL solution. Proteoliposome preparations were stored at 4 °C under an argon atmosphere for up to 48 h before use with no further treatment.

Glycophorin A membrane protein was used in lieu of membrane-bound gangliosides, such as GD1a (1) because we found that the H1N1 virus strain did not become immobilized upon planar bilayers when sialic acid was presented in this fashion, including use of ganglioside mixtures (catalog no. 345717;

Calbiochem) and S-Sialyl-a(2,6)-lactosylceramide (Wako Pure Chemical Industries). Both the H1N1 and H3N2 virus strains used bound to planar bilayers comprising the GYPA membrane protein, although the numbers of immobilized viruses exhibited a substantial amount of fluctuation between experimental runs (Fig. S2). The requirement by H1N1 to use GYPA rather than a ganglioside for immobilization also reduced the degree of control over the amount of sialic acid receptor on the bilayer surface because each GYPA protein contains multiple sialic acid moieties.

Microscope Specifications. Measurements were conducted on an inverted fluorescence microscope (Olympus IX-71) equipped with a custom-ordered microscope filter cube (filters zet488/561m and zt488/561rpc; Chroma Ltd.) and either a 60× N.A. 1.49 objective (Olympus APON60OTIRF) or a 60× N.A. 1.45 objective (PLANAPON60TIRF; Olympus). The N.A. 1.45 objective was found to exhibit less chromatic aberration at the edge of the images, improving the colocalization between the virus and IgG/Fab signal. Virus particles and labeled IgG/Fab were illuminated, respectively, with ~0.25 W/cm^2 561-nm and ~0.2 W/cm^2 488-nm continuous-wave solid state lasers (Sapphire models; Coherent, Inc.) focused onto the back-focal plane of the microscope objective and aligned in objective-based TIR mode. The configuration was optimized to homogeneously illuminate the entire virus particle and the fluorescence intensity of labeled IgG/Fab bound to viruses was found to be independent at TIR incidence angles less than 57° (Fig. S5), while still suppressing background fluorescence. Emitted green and red fluorescence was separated by a home-built dual-view system with a Thorlabs DMLP567 long-pass filter or by a commercial Dual-View system (Photometrics) with a Chroma T560LPXR long-pass filter. Signals were filtered to remove stray laser light and background from Raman scattering (Chroma ET525-50m and ET605-70m, green and red respectively), then focused onto either half of an electron-multiplying CCD camera (Image-EM model C9100-13; Hamamatsu Photonics K.K.). False-color representative images resulting from this setup are depicted in Fig. 1.

Fusion Experiment. Glass-supported planar bilayers were formed by adding the proteoliposome solution to a HNE-hydrated microfluidic flow cell mounted on the microscope and incubated with the glass surface for a minimum of 45 min at room temperature. R18-labeled viruses were diluted 10-fold into a solution of 100% Alexa-488–labeled IgG/Fab, bringing the IgG/Fab to the desired final concentration. We estimate a virus particle concentration of ~6 × 10^{12} per milliliter during IgG/Fab incubation, calculated using previous measurements that 37% of the total virus protein is HA (5) and that there are 375 HA trimers per virus (6, 7). This concentration was found to be the most dilute concentration of virus that allowed for sufficient virion immobilization on the bilayer surface while gathering reasonable statistics. Virus and IgG/Fab were incubated for 45–60 min at room temperature, and then added to the microfluidic flow cell at 5 μL/min, wherein the viruses immobilized on the planar bilayer through specific HA–GYPA interactions. Fluorescein-labeled streptavidin (Invitrogen) was subsequently added at 0.2 μg/mL using a flow rate of 10 μL/min for 5 min; therein the labeled IgG/Fab not bound to viruses washed away to leave a low background. A 2-min wash with clean HNE buffer at a high (100 μL/min) rate removed unbound viruses, IgG, and streptavidin-fluorescein. Finally, viral fusion was initiated by rapid injection of a citric acid buffer (10.0 mM citric acid, 140 mM NaCl, 0.2 mM EDTA, pH 5.0) at 200 μL/min and recorded using Metavue imaging software (Life Science Imaging Ltd.) at an acquisition rate of 5 Hz for 240 s and maximal EM gain. Laser illumination during the first 5–6 s and before the pH drop was with 561 nm only, then the 488-nm illumination was initiated. This alternation allowed for identification of viruses in the red channel, then

colocalization in the green channel. Total laser illumination was ~400 mW/cm^2 and was set such that at high neutralizing molecule concentration there were very few saturated pixels together with a large range of pixel intensity values. Following immobilization of the virus on the bilayer surface, the fusion experiments required 10–20 min total experimental time.

Data Extraction and Analysis. The laser illumination profile in each channel was identified after the pH drop by smearing out fluorescent peaks with a 40-pixel radius median filter, which allowed for the fitting of the underlying beam profile with a 2D Gaussian. The fitted profile was set to have a maximal value of one at its peak. Each image extracted from the recording was corrected for the illumination profile (flattened) by first removing dark counts and then dividing by the fitted profile.

Individual viral particles were identified and their fluorescent trajectories extracted using a custom MATLAB code similar to that described previously (1). The arrival of the low-pH buffer was detected, as previously described (1), as a sudden loss of fluorescein signal in the green channel. Red-channel fluorescence peaks were identified by averaging 10 frames under 561-nm illumination only, flattening and removing global fluorescence background (see below), and then applying a discoidal averaging filter (8). Peaks were identified by thresholding using a μ + 2 × σ criterion, where μ and σ are the average intensity and intensity SD, respectively, of the filtered red channel. Greenchannel peaks were similarly identified by averaging 10 frames after the pH drop. Colocalization was achieved by translating the locations found in the red channel onto the green channel and grouping the nearest-neighbor pairs of peaks.

Peaks in the green channel were fit with a 2D Gaussian profile and all pixels within 3σ of the peak center were identified for signal integration; red-channel peaks were surrounded with a 4 × 4-pixel square box for fluorescence signal integration. Fluorescence background in the green channel was identified on a perparticle basis as the baseline offset resulting from Gaussian fitting, whereas the red-channel background was found globally by taking the peak of the distribution of the pixel intensities from the flattened image used for particle colocalization.

Red-channel fluorescent trajectories were plotted and manually selected as exhibiting hemifusion similar to previous description (1). Those showing clear dequenching spikes followed by dissipative signal loss, as shown in the Fig. 1B, were directly classified as fusing virions. Trajectories showing characteristics of dequenching and/or dissipative signal loss, but that were not as overtly similar to the trajectory of Fig. 1B, were subjected to further manual inspection. In these cases, a virus particle in question is observed in the recorded fusion movie and those showing a rapid, outward movement of R18 molecules away from the virus identifiable by eye were also classified as fusing virions. Absolute hemifusion efficiency in each experiment was calculated as the number of particles in a field of view determined to undergo hemifusion divided by the total number of particles initially detected in the same field of view. Hemifusion efficiency data were fit using a four-parameter logistic model using the transform-both-sides approach for variance stabilization (9) using a logit transformation (Table S2, Eq. **S1**). For fitting, conditions with no fusion events were set to one event.

The integrated green-channel fluorescence corresponding to the virus-bound-labeled IgG/Fab was averaged over 15 frames (3 s), starting five frames (1 s) after the pH drop (dark green square in Fig. 1C). Separately, the average integrated intensity of individual labeled IgG or Fab molecules was obtained by nonspecifically adsorbing them to a clean glass surface within a microfluidic channel and measuring their fluorescence intensity under identical illumination conditions as used in the fusion experiments (Fig. S5). Laser power was varied to ensure fluorophore

excitation occurred within the linear response regime (Fig. S5) and to obtain photobleaching data (Fig. S3).

The number of molecules bound to HA on the surface of each virus was calculated by dividing the average integrated fluorescence intensity measured from the fusion experiments by the average integrated intensity measured for individual IgG/Fab molecules. When determining the intensity corresponding to individual IgG/Fab molecules, the illumination conditions were such that fluorescence intensity was independent of the TIRF angle and was linearly dependent upon the incident laser power density (Fig. S5). In standard TIRF microscopy, the illumination beam has penetration depths near 200 nm into the sample. We chose a TIRF angle of 57° that was far from the critical angle of 61° required for TIR. As a result, excitation light propagated through the sample at a highly inclined angle, rather than undergoing reflection. This illumination design is similar to highly inclined and laminated optical sheet microscopy (10). Therein, Tokunaga et al. imaged samples at depths of 15 μm with only 40% loss of fluorescence intensity, whereas we imaged our ~120-nm viruses at penetration depths ~100-fold lower. Our shallow imaging depth combined with our illumination angle far from the critical angle would suggest that the rapidly decaying penetration depth relevant to standard TIRF microscopy is not likely to significantly affect our measurements.

The value for the number of IgG/Fab bound to each virus was corrected for the presence of unlabeled IgG/Fab using the visualized fraction measured by MALDI and photobleaching (Table S1). To this end, the number of IgG/Fab calculated to be bound to each virion was multiplied by a correction factor corresponding to one divided by the visualized fraction. We have used the correction factor found using the average number of dyes per IgG/Fab molecule. Using only the result from photobleaching measurements would result in 0.7–6.9% additional IgG/Fab bound to the viruses (2.8% average), whereas using only the MALDI result would result in 0.3–3.2% fewer IgG/Fab bound to the viruses (1.4% average). For each experimental run, the distribution for the numbers IgG/Fab bound to all virions (both fusing and nonfusing) was corrected for unlabeled IgG/Fab and its median value calculated (Fig. 2). The median values for the numbers of IgG/Fab bound were fit with a hyperbola using the transform-both-sides approach for variance stabilization (9) using a square-root transformation (Table S2, Eq. **S2**).

Numbers of IgG/Fab were related to hemifusion efficiency by the following: For a given number of bound IgG or Fab, the corresponding IgG/Fab concentration was estimated and used to estimate the corresponding hemifusion efficiency with 95% confidence interval (error propagation using proc NLMIXED Version 9.2; SAS), using the delta method (11, 12) and the lowest degrees of freedom from the two models.

Hemifusion time to event for each particle was determined as the elapsed time between the pH-drop frame and the frame when hemifusion occurs, defined as the time point with the maximal rate of fluorescence increase. The time-to-hemifusion distribution for each experimental run was determined and its geometric mean time and geometric SD (error) determined. The geometric mean was used to preserve the semilog distribution, often used to analyze waiting time distributions (13). The times resulting from each experiment were $\log_{10}$ transformed and fitted by a hyperbola with a constant offset (Table S2, Eq. **S3**). The geometric means in the absence of IgG/Fab reported in *Results* (46 s for H1N1; 30 s for H3N2) are comparable to estimates obtained from data fitting (Table S2), indicating our models were properly anchored.

Distributions of hemifusion times that we have obtained previously (1) and in the current work (Fig. S8) show a rise and decay in the frequency of events. As described in Floyd et al. (1) such an observation indicates that hemifusion does not occur through a single, one-step biochemical transition, rather that intermediate states exist in the biochemical process leading to hemifusion. In the previous work of Floyd et al. (1), we used the gamma distribution to obtain estimates for the rate of the rate-limiting step in the hemifusion process, k, and the number of independent steps that must be present for hemifusion to occur, N:

$$P(t|k,N) = \frac{k^N t^{N-1}}{\Gamma(N)} \exp(-kt).$$

Floyd et al. reported that $N > 1$ and that this trend was independent of proton concentration, which triggers the HA to unfold and mediate fusion. Such an observation is consistent with N independent steps acting in parallel, each with rate k, and, therefore, that the N parameter corresponds to the number of HA trimers reacting to low pH (high proton concentration) to mediate hemifusion.

Fit parameters for the gamma distribution found for hemifusion times measured here in the presence of IgG/Fab are presented in Fig. S8. There, the N parameter does not drop below 1, staying in the range of 2 to 3 as observed previously (1). We therefore conclude that $N > 1$ at both limiting proton concentrations (1) and following removal of fusogenic HA trimers (Fig. S8). As discussed in the main text, only experimental runs where 50 or more hemifusion times were obtained were used for analysis by fitting with this distribution, in accord with supplemental reference (14). Fit parameters were calculated, equivalently, using fitting standard algorithms in SAS statistical software or in MATLAB (gamfit function).

Monte Carlo Simulation. To simulate protein packing on the viral surface we used a simple 2D model. Model viral surfaces were generated using a Monte Carlo algorithm minimizing protein overlap and maximizing IgG/Fab–HA interactions. Each protein was approximated with a number of spheres (Fig. S7) such that their final dimensions were in agreement with appropriate crystal structures. Model viral membranes were composed of the envelope-embedded proteins HA, neuraminidase (NA), and M2 proton channel. Binding geometry of IgG/Fab to the HA proteins was constrained to be in agreement with the CR8020-HA cocrystal structure [PDB ID code 3SDY (15)].

IgG molecules (14 nm in total length) containing two paratopes were modeled with the Fc domain pointing vertically from the in silico viral surface and were allowed to have flexibility around their midpoint. They were constructed from five spheres: two for each fab, one representing the variable and the other the constant region, and one sphere corresponding to the Fc tail. Fab fragments (7 nm in length) were not flexible, had a single paratope, and were constructed from two spheres. HA was approximated with four spheres: one larger for the stem and three for the HA1 heads. The diameter of the HA stem was measured around the epitope area of the CR8020 antibody to assure correct binding geometry. The approximate size of the extracellular domain of the M2 proton channel was estimated from its the molecular mass, accounting for the protein's tetrameric quaternary structure. NA was modeled as a single sphere. The spike protein (HA and NA) density was set at 8,000 spikes per square micron and an HA:NA ratio of 7:1 in agreement with previous studies of similar influenza virus samples (6, 7). From this density, a surface representing our average 125-nm virus particles contained 392 spike proteins, 341 of which were HA.

Simulations were performed by placing viral proteins randomly within a 2D periodic simulation surface. The surfaces were minimized with a Monte Carlo-like algorithm to remove protein overlap from a randomly generated surface. The overlap energy was modeled as a square-well potential with an additional term proportional to the overlap surface. Increasing IgG/Fab concentrations were added and their final structure and position

determined using the Monte Carlo sampling. The paratope–epitope interaction energy was modeled using the patchy-spheres approach (16) so as to impose appropriate distances and angles between the epitope and paratope as dictated by their cocrystal structure (15). We found that using a smooth potential instead of a square-well interaction energy allowed Monte Carlo minimization to converge faster due to the longer range of protein–protein interactions. For the minimization we used the following moves: single protein rotation and perturbation, two proteins swapping, IgG/Fab jumping to another binding site, and randomizing Fab–Fab angle of the IgG. The IgG/Fab concentration at which protein overlap could not be prevented was taken as the steric packing limit.

We then used the viral surfaces to calculate the number of available binding sites parameter. This calculation was done by placing a sample IgG/Fab at every HA epitope, checking if the molecule could be placed without overlap, and summing the number of epitopes permitting the additional IgG/Fab. Also for the antibody, multiple Fab–Fab angles were tested. The number of available binding sites calculated in this manner was then averaged over the whole set of surfaces as a function of ligands already bound to the virus (Fig. S7).

Previous studies have argued that groups of HA in close proximity could represent fusogenic clusters that cause nucleation of membrane fusion events (17). Simulation data were analyzed to identify HA clusters defined to be groups of HA trimers free from IgG/Fab that were in close proximity to each other without any additional surface proteins between them; cluster disruption was defined to occur when these conditions were not met. Unfortunately defining clusters of fixed sizes from three to six neighboring HA trimers did not result in replication of trends observed in the experimental data of hemifusion efficiency, namely a need for more Fab than IgG to achieve equal cluster disruption, and the results of these analyses are not included.

1. Floyd DL, Ragains JR, Skehel JJ, Harrison SC, van Oijen AM (2008) Single-particle kinetics of influenza virus membrane fusion. *Proc Natl Acad Sci USA* 105(40): 15382–15387.
2. Delamarche E, Bernard A, Schmid H, Michel B, Biebuyck H (1997) Patterned delivery of immunoglobulins to surfaces using microfluidic networks. *Science* 276(5313):779–781.
3. Xia Y, Whitesides G (1998) Soft lithography. *Annu Rev Mater Sci* 28:153–184.
4. Brandenburg B, et al. (2013) Mechanisms of hemagglutinin targeted influenza virus neutralization. *PLoS ONE* 8(12):e80034.
5. Tiffany JM, Blough HA (1970) Models of structure of the envelope of influenza virus. *Proc Natl Acad Sci USA* 65(4):1105–1112.
6. Harris A, et al. (2006) Influenza virus pleiomorphy characterized by cryoelectron tomography. *Proc Natl Acad Sci USA* 103(50):19123–19127.
7. Harris AK, et al. (2013) Structure and accessibility of HA trimers on intact 2009 H1N1 pandemic influenza virus to stem region-specific neutralizing antibodies. *Proc Natl Acad Sci USA* 110(12):4592–4597.
8. Hedde PN, Fuchs J, Oswald F, Wiedenmann J, Nienhaus GU (2009) Online image analysis software for photoactivation localization microscopy. *Nat Methods* 6(10): 689–690.
9. Findlay JW, Dillard RF (2007) Appropriate calibration curve fitting in ligand binding assays. *AAPS J* 9(2):E260–E267.
10. Tokunaga M, Imamoto N, Sakata-Sogawa K (2008) Highly inclined thin illumination enables clear single-molecule imaging in cells. *Nat Methods* 5(2):159–161.
11. Billingsley P (1986) *Probability and Measure* (John Wiley & Sons, Inc., New York).
12. Cox C (1998) *Encyclopedia of Biostatistics*, eds Armitage P, Colton T (John Wiley, New York), pp 1125–1127.
13. Limpert E, Stahel W, Abbt M (2001) Log-normal distributions across the sciences: Keys and clues. *Bioscience* 51(5):341–352.
14. Floyd DL, Harrison SC, van Oijen AM (2010) Analysis of kinetic intermediates in single-particle dwell-time distributions. *Biophys J* 99(2):360–366.
15. Ekiert DC, et al. (2011) A highly conserved neutralizing epitope on group 2 influenza A viruses. *Science* 333(6044):843–850.
16. Huisman BA, Bolhuis PG, Fasolino A (2008) Phase transition to bundles of flexible supramolecular polymers. *Phys Rev Lett* 100(18):188301.
17. Bentz J (2000) Minimal aggregate size and minimal fusion unit for the first fusion pore of influenza hemagglutinin-mediated membrane fusion. *Biophys J* 78(1):227–245.
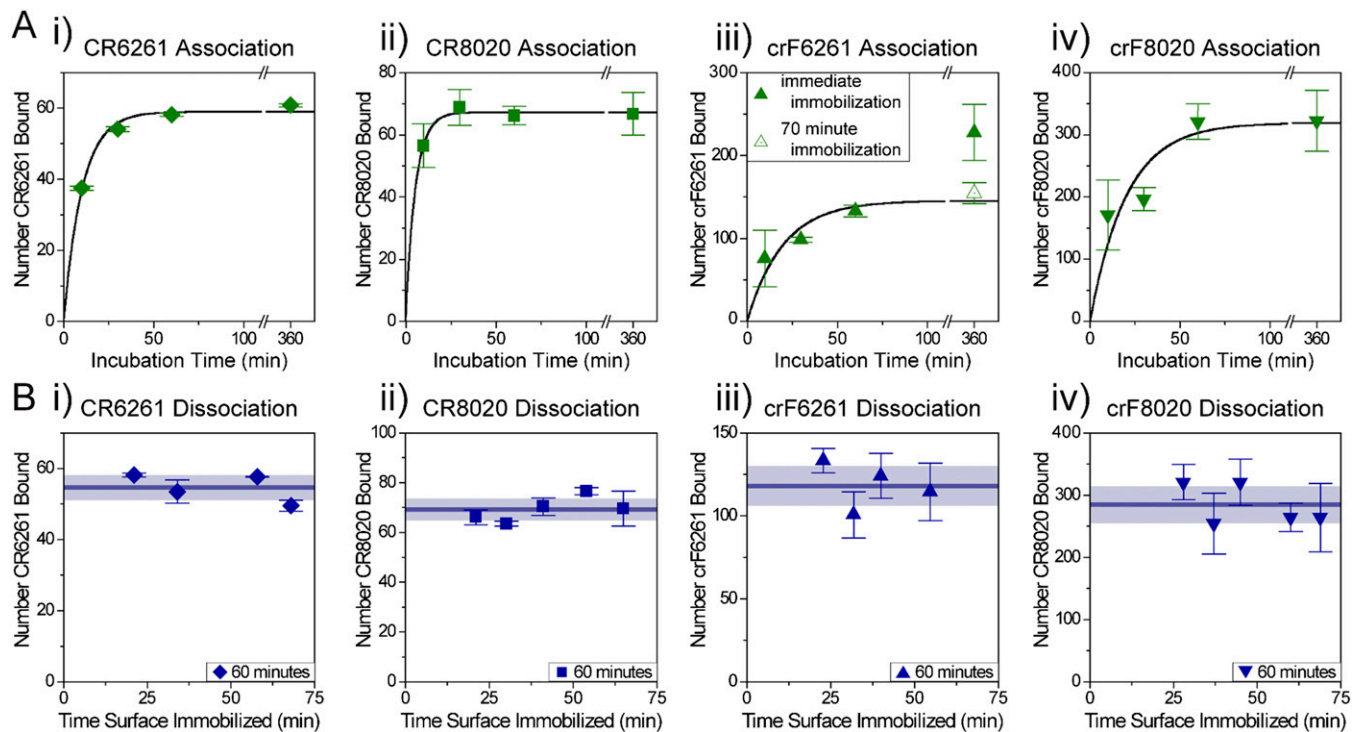
Fig. S1. Association (*A*) and dissociation (*B*) of CR6261 (*i*) and CR8020 IgG (*ii*), and of crF6261 (*iii*) and crF8020 Fab (*iv*). For IgG/Fab association plots, H1N1 (*A, i* and *iii*) or H3N2 (*A, ii* and *iv*) viruses were incubated with 130 nM IgG or Fab for the time indicated on the horizontal axis, then added to flow channels to become immobilized on the supported lipid bilayer (SLB). Flow-in time of the virus plus IgG/Fab solution was ~20 min. Two fields of view were imaged in rapid succession and the average IgG/Fab coverage ± SEM is reported. (*B*) For dissociation after immobilization, IgG/Fab coverage on the same virus samples as in *A* were quantified at ~10 to 20-min intervals without repeated imaging of the same fields of view. Fusion experiments described in the main text typically had a run time of 10 min after flow-in of the virus-IgG/Fab solution. For clarity, only dissociation measurements corresponding to 60 min incubation (blue) from *A* are shown. Mean values of the number of bound IgG/Fab ± SD over the times after immobilization are indicated by the horizontal line and shaded regions, respectively. Fluorescence intensity fluctuated between fields of view, as indicated in the scatter of the data points, but did not systematically decrease as would be expected if nonspecific binding occurred or if the IgG/Fab otherwise dissociated from the virus. Nonspecific binding occurred only for 360 min incubation of crF6261 with H1N1 (filled symbol at 360 min in *A, iii*), which was observed to systematically decrease to coverage levels equivalent to 60-min incubation (open-faced symbol at 360 min in *A, iii*) after 70 min of immobilization on the SLB surface.
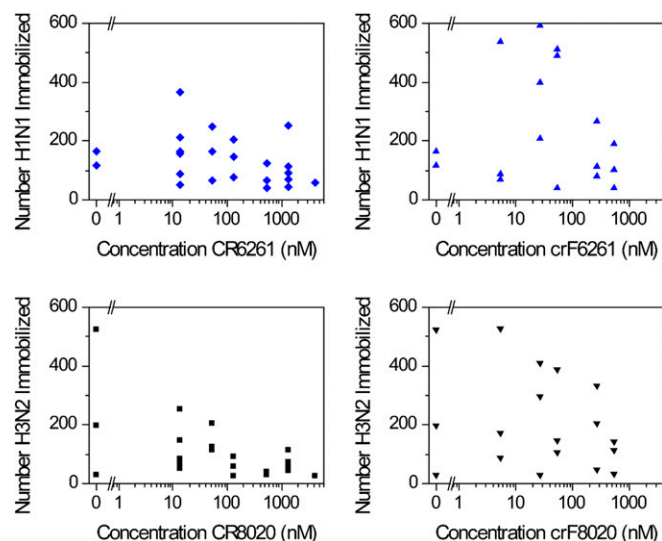

Fig. S2. Immobilization of the virus to target bilayers through glycophorin A binding was largely unaffected by IgG/Fab binding to the viral surface. Each data point corresponds to a single fusion experiment and represents the total number of virions imaged in equal-sized fields of view. Although there is some decrease in binding at the highest concentrations, many virions are still visualized, indicating that IgG/Fab binding does not prevent HA-receptor recognition.
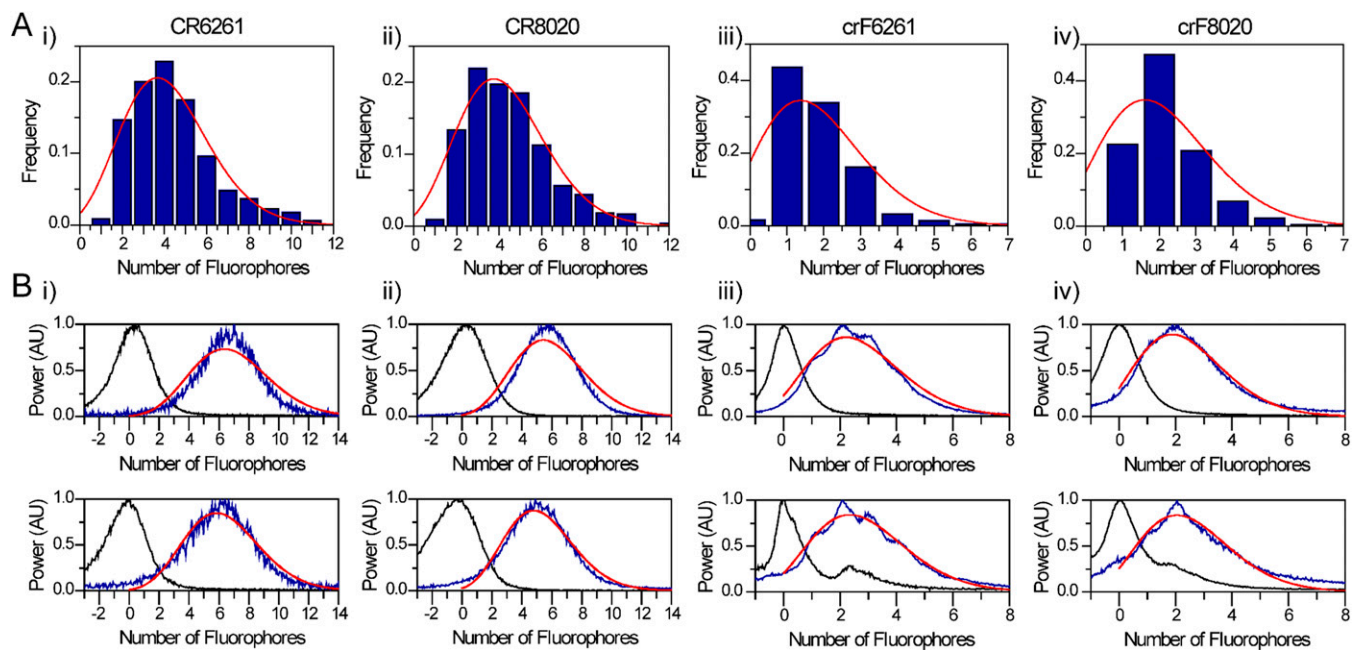
Fig. S3. Degree of Alexa-488 labeling for 6261 IgG (*i*) and Fab (*ii*), and for 8020 IgG (*iii*) and Fab (*iv*), as measured by photobleaching analysis (*A*) and MALDI mass spectrometry (*B*). (*A*) Photobleaching measurements resolved the distribution of number of Alexa-488 molecules bound to each molecule as described in *SI Materials and Methods*. These distributions were fit with a Poisson distribution (red lines) to identify the expected number of fluorophores bound to each IgG/Fab. (*B*) Mass spectra at mass:charge ratios of 1 (*Top*) and 2 (*Bottom*) were determined for the unlabeled IgG/Fab (black) and for the Alexa-488–labeled IgG/Fab (blue). The peak value from the unlabeled spectra was subtracted from each labeled spectra, and then each spectra was divided by the molecular mass of Alexa-488. The mass spectra of the labeled molecules were fit with a Poisson distribution (red) to identify the expected number of fluorophores covalently linked to each IgG/Fab. Spectra for Fab molecules resolved identifiable peaks corresponding to molecules having one, two, three, and four dye molecules (*B*, *iii* and *iv*). Results of fitting are summarized in Table S1.
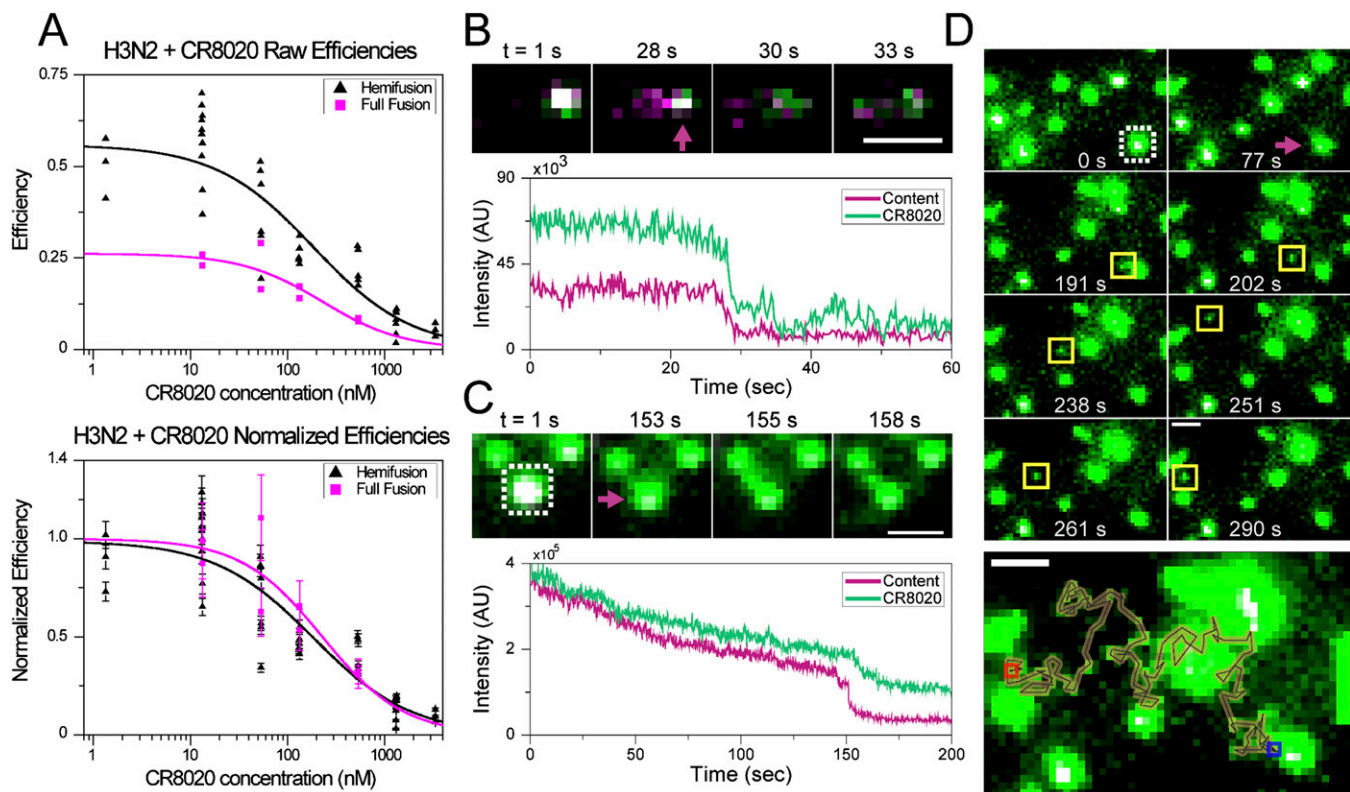
Fig. S4. CR8020 binding inhibits full fusion as well as it does hemifusion. The luminal contents of H3N2 viruses were labeled with aqueous sulforhodamine B dye, as described previously (1), and the viruses subsequently incubated with Alexa-488–labeled CR8020 IgG. Planar bilayers were formed in a microfluidic chamber on either dextran-functionalized glass coverslips (1) or PEG-functionalized glass coverslips where 5% of the PEG used was covalently coupled to the phospholipid 3-(*N*-succinimidyloxyglutaryl) aminopropyl, polyethyleneglycol-carbamyl distearoylphosphatidyl-ethanolamine (DSPE) (2, 3). Bilayer composition was supplemented with 1% molar fraction of the ganglioside Gd1a to allow virus immobilization. Upon pH drop, the viruses underwent full membrane fusion visualized as a loss of content dye from the viral lumen, indicating that a full fusion pore had formed (1). (*A, Top*) Increasing concentrations of CR8020 decreases the efficiency of full fusion (magenta squares). The hemifusion efficiency data (black)—aggregated from the data shown in Fig. 2*A* together with data previously reported (4) —is shown for comparison; full fusion shows a lower overall efficiency compared with hemifusion. (*A, Bottom*) Full fusion and hemifusion data were normalized to their respective efficiencies in the absence of CR8020. Best-fit lines using Eq. **S1** in Table S2 show good overlap between the two functional read outs and indicate that hemifusion inhibition is an appropriate read out for full fusion inhibition. (*B–D* and Movies S1–S3) Some viruses, which were bound by a subinhibitory number of CR8020 IgG molecules, showed outward diffusion of HA–CR8020 complexes into the DSPE–PEG-supported bilayer shortly after full fusion. Viruses were observed to fully disintegrate (*B* and Movie S1), partially disintegrate (*C* and Movie S2), or release only a small cluster of HA-CR8020 (*D* and Movie S3) following full fusion. The virus particle of interest is highlighted by a white, dashed box in *C* and *D*. In all images, SRB fluorescence from the viral lumen is colored in magenta, CR8020 fluorescence is colored in green, overlap between the two is seen as white. (Scale bars: 2 μm.) The first image of the montages (*t* = 0 or 1 s) demonstrate colocalization of the two fluorescence signals, and the full fusion event is marked with a magenta arrow in the second image (*t* = 28, 153, and 77 s, respectively). Subsequent montage images depict outward diffusion of HA in complex with CR8020. In *B* and Movie S1, labeling of the viral lumen by SRB was sufficient in this virus to allow visualization of the SRB molecules as they diffuse in the space between the glass coverslip and the tethered bilayer after full fusion. *B* and *C* include fluorescence trajectories from the virus particles of interest and show loss of the CR8020 fluorescence corresponding to full (*B* and Movie S1) or partial (*C* and Movie S2) disintegration of the viruses after the full fusion event. *D* shows an image montage from Movie S3 where, after full fusion (*t* = 77 s), a small HA–CR8020 cluster breaks off from the virus particle (*t* = 191 s, yellow square) and undergoes long-range, 2D diffusion. Below the image montage is the path of this small HA–CR8020 cluster overlaid on top of a maximum-intensity projection of Movie S3. The cluster's diffusional movement starts at the blue square near the virus particle on the lower right of the image and ends at the red square on the left. Note that for observing full fusion here, the bilayers were supported by PEG or dextran-functionalized coverslips to separate the lower bilayer leaflet (viewed from the side in Fig. 1*B*) from the glass surface. This design prevents interactions between the glass and the lipid bilayer, and creates an aqueous space for viral content release. When observing hemifusion, as in the main text, the lipid bilayer was formed on glass alone for experimental simplicity. This design was previously shown to provide equivalent kinetic hemifusion data (1) as fusion to a cushioned bilayer because the upper leaflet is equally fluid. In this latter experimental design, interaction between the bilayer lower leaflet and the glass prevents outward diffusion of both the GYPA and HA after fusion. As such, the HA–IgG signal does not disappear following hemifusion in our experimental design because the HA–IgG complex cannot diffuse away from the site of fusion.

1. Floyd DL, Ragains JR, Skehel JJ, Harrison SC, van Oijen AM (2008) Single-particle kinetics of influenza virus membrane fusion. *Proc Natl Acad Sci USA* 105(40):15382–15387.
2. Reich C, Andruzzi L (2010) Preparation of fluid tethered lipid bilayers on poly(ethylene glycol) by spin-coating. *Soft Matter* 6(3):493–500.
3. Mashaghi S, van Oijen AM (2014) A versatile approach to the generation of fluid supported lipid bilayers and its applications. *Biotechnol Bioeng* 111(10):2076–2081.
4. Brandenburg B, et al. (2013) Mechanisms of hemagglutinin targeted influenza virus neutralization. *PLoS ONE* 8(12):e80034.
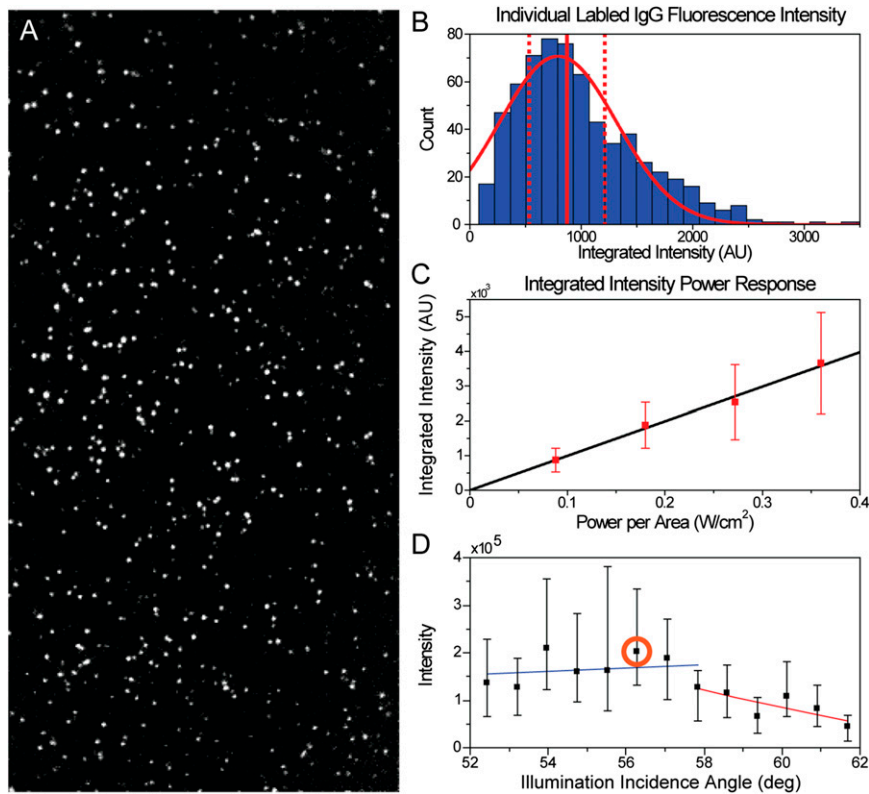
Fig. S5. Imaging of individual, labeled IgG molecules. (*A*) Representative image of CR8020af488-labeled IgG molecules adsorbed to a clean glass surface, visualized at ~0.1 W/cm^2 in pH 5.0 citric acid buffer, averaged over 100 frames acquired at 200 ms exposure time, and corrected for the Gaussian laser beam illumination profile. Image size is 512 × 256 pixels (140 × 70 μm). (*B*) Distribution of integrated fluorescence intensities acquired from *A*. The distribution is well fitted by a Gaussian distribution (red curve, R^2 = 0.932). The median value of this distribution (solid vertical line ± median absolute deviation, dashed lines) is taken as the integrated fluorescence intensity per IgG/Fab molecule used in calculating the number of bound IgG/Fab. (*C*) Median values of the averaged integrated fluorescence intensities, as measured in *B*, increases linearly with increasing laser illumination power, indicating that fluorescence read out of individual labeled IgG/Fab is linearly dependent on illumination input. (*D*) The angle of incidence of the excitation lasers upon the glass–water interface (horizontal axis) was varied to measure the fluorescence intensity (vertical axis) of CR8020af488 IgG bound to H3N2 virus incubated with 130 nM IgG and immobilized on a glass-supported bilayer. As expected, TIR occurred near 61° relative to the axis perpendicular to the glass surface. Data points are median values ± interquartile range. For angles smaller than 57°, the fluorescence intensity varied only slightly (blue line), indicating a homogenous evanescent field over the length scale of a virus. The effect of the evanescent wave was apparent for larger incidence angles (red line). The TIR angle was set to ~56° (orange circle) for all experiments to minimize the effect of the evanescent field but still achieve high signal-to-background recordings (*A* and Fig. 1*A*).
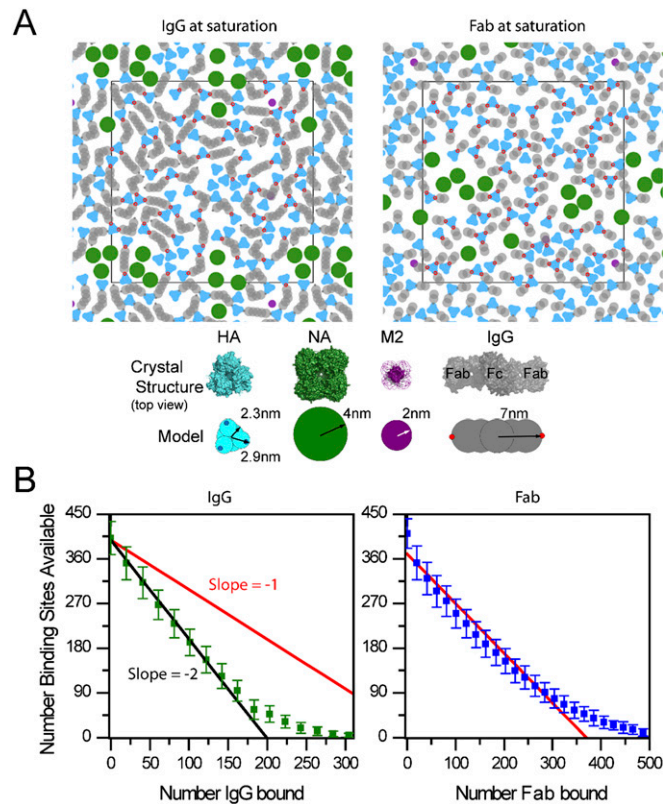
Fig. S6. Transmission EM of influenza strains H1N1 and H3N2. (*A*) H1N1 and H3N2 viral strains were diluted 1 million-fold to obtain nearly isolated particles and avoid deformation from virus–virus contact, then negatively stained with uranyl acetate on a carbon-coated TEM grid, and imaged at 45,000× magnification. In total, 19 of the 22 H1N1 viruses and 20 of the 26 H3N2 viruses imaged were used for diameter measurements. Both virus strains were spherical in appearance and generally had high surface spike protein density. Diameters of the virus particles were measured at the base of the spike proteins in the area of high contrast surrounding the virus, indicated by the yellow circle in the image. (*B*) Box plot of the diameters of the H1N1 (blue) and H3N2 (black). The square data point and vertical line inside the box represent the mean and median diameters, respectively. Left and right edges of the box are the 25th and 75th percentiles, respectively, and similarly the left and right whiskers are the first and 99th percentiles, respectively.

Fig. S7. Monte Carlo simulations of protein packing on a viral surface. (*A*) Simulated binding at full saturation when all binding sites are occupied by IgG (*Left*) or by Fab (*Right*). Simulations represented relevant proteins whose size corresponds to their crystallographic dimensions when viewed from the top, looking down on a viral surface. HA is in cyan, NA is in green, the M2 proton pump is in violet, and IgG (or Fab) is in gray. The spike protein (HA or NA) density shown corresponds to 8,000 spikes per square micron with a 7:1 ratio of HA:NA. Epitopes on the HA that are engaged with IgG or Fab paratopes are depicted as small, red circles. (*B*) The number of sterically available epitopes (vertical axis) diminished as the number of IgG (*Left*, green) or Fab (*Right*, blue) molecules on the viral surface increased. We see that no epitopes are sterically available when ~270–300 IgG or ~500 Fab molecules are bound. To approximate the rate of epitope loss upon IgG/Fab binding, lines having slopes of −2 (black) and −1 (red) are included. For IgG, the data closely follows the black line until ~175 IgG are bound, suggesting that IgG binds with both paratopes to remove two binding sites up to this point. Beyond this region the rate of epitope loss deviates substantially from the black line (slope = −2), suggesting that each additional IgG does not bind with both paratopes. A majority of the Fab data are roughly parallel to the red line, as would be expected for single-paratope binding and low amounts of steric interactions, until more than ~300 Fab had bound. We note that we have used only a single-spike density and HA:NA ratio leading to 375 total HA trimers on the viral surface, in accord with previous estimates for virus samples obtained through identical virus particle harvesting methods (1, 2). The polymorphic shape of other influenza viruses (not represented in our samples) could cause variation in the total number of HA present.

1. Harris A, et al. (2006) Influenza virus pleiomorphy characterized by cryoelectron tomography. *Proc Natl Acad Sci USA* 103(50):19123–19127.
2. Harris AK, et al. (2013) Structure and accessibility of HA trimers on intact 2009 H1N1 pandemic influenza virus to stem region-specific neutralizing antibodies. *Proc Natl Acad Sci USA* 110(12):4592–4597.
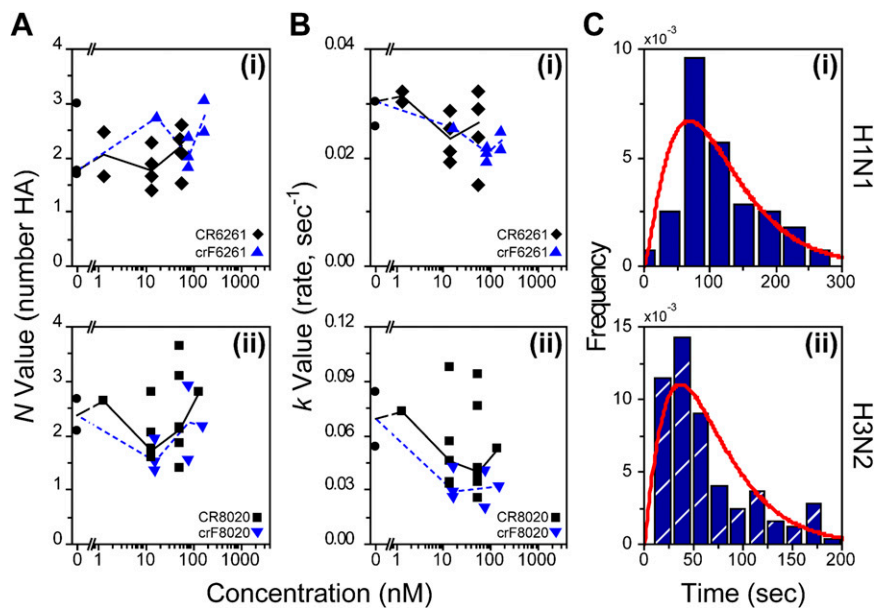
Fig. S8. Gamma distribution analysis of hemifusion times reveals a constant number of HA trimers needed for hemifusion at low and medium IgG/Fab coverage. (*Top*) Data is designated with *i* is for H1N1 bound by CR(F)6261 and (*Bottom*) *ii* is for H3N2 bound by CR(F)8020. Data points for IgG are in black and for Fab in blue; fit parameters in the absence of IgG/Fab are shown as circles in each plot. Median *N* (*A*) and *k* (*B*) values for each IgG or Fab concentration are connected by a solid black line or dashed blue line, respectively, and serve as a guide to visualize trends in the data. (*A*) The *N* parameter is interpreted to be the number of HA trimers participating in the membrane fusion process (1). Here we see that for both H1N1 (*A, i*) and H3N2 (*A, ii*), the number of HA required for fusion remains constant, between two and three, as IgG/Fab concentrations increase. This observation indicates that multiple HA are always required for hemifusion to occur. (*B*) The rate of the rate-limiting step in the fusion reaction is observed to decrease at higher IgG/Fab concentrations, in accord with data in Fig. 3. In addition, the H1N1 strain (*B, i*) is found to be slower than the H3N2 strain (*B, ii*), in agreement with Fig. 3. These kinetic behaviors are better demonstrated in Fig. 3 where all experimental data are shown, without a lower limit for number of events. (*C*) The hemifusion-time event-frequency distributions are shown for individual, representative experiments of H1N1 bound by crF6261 (*C, i*) and for H3N2 bound by crF8020 (*C, ii*) at concentrations of 160 nM Fab (blue) together with the corresponding gamma distribution fit curve (red). The rise-and-decay behavior is evident in the distribution even at this high Fab coverage, indicative of multiple kinetic steps being required for hemifusion to occur, as previously reported (1).

1. Floyd DL, Ragains JR, Skehel JJ, Harrison SC, van Oijen AM (2008) Single-particle kinetics of influenza virus membrane fusion. *Proc Natl Acad Sci USA* 105(40):15382–15387.

Table S1. Degree of IgG/Fab labeling and percent visualized

Fusion-inhibiting molecule	Photobleaching		MALDI mass spectroscopy					Dyes per molecule $\pm$ SEM	Percent visualized[†]
	λ*	R^2	λ, m/z = 1*	R^2	λ, m/z = 2*	R^2	$<\lambda> \pm$ SEM		
CR6261	4.2 $\pm$ 0.1	0.950	6.87 $\pm$ 0.03	0.934	6.34 $\pm$ 0.03	0.959	6.6 $\pm$ 0.2	5.4 $\pm$ 0.8	99.5 $\pm$ 0.4
CR8020	4.3 $\pm$ 0.1	0.958	5.94 $\pm$ 0.02	0.955	5.29 $\pm$ 0.02	0.978	5.6 $\pm$ 0.2	5.0 $\pm$ 0.5	99.3 $\pm$ 0.3
crF6261	1.9 $\pm$ 0.2	0.850	2.73 $\pm$ 0.01	0.974	2.86 $\pm$ 0.02	0.941	2.80 $\pm$ 0.05	2.4 $\pm$ 0.3	91 $\pm$ 3
crF8020	2.1 $\pm$ 0.2	0.881	2.39 $\pm$ 0.01	0.964	2.56 $\pm$ 0.03	0.853	2.48 $\pm$ 0.06	2.3 $\pm$ 0.1	90 $\pm$ 1

*Results for Poisson distribution [$p(k,\lambda) = A \times (\lambda^k) \times \exp(-\lambda)/\Gamma(k + 1)$] fits from Fig. S3, where *A* was unconstrained to allow for various amplitudes; parameter errors are those reported by OriginLab plotting software during χ^2 minimization using mean residual variance and the parameter covariance matrix.
[†]Percent visualized corresponds to the percentage of labeled IgG/Fab molecules bound with at least one fluorophore. Error is calculated by error propagation for a Poisson distribution.

Table S2. Fit lines and corresponding estimated parameters determined by fitting data points from all experimental runs

Data and fit model	Parameter	H1N1		H3N2	
		CR6261	crF6261	CR8020	crF8020
Hemifusion efficiency [$E(c)$]	A	0.006 (−0.009, 0.021)	0.011 (−0.001, 0.023)	0.033 (−0.005, 0.072)	0.033 (0.017, 0.049)
$\mathrm{logit}[E(c)] = \mathrm{logit}\left[D + \dfrac{A-D}{1+\left(\frac{c}{10^{C_0}}\right)^p}\right]$ [S1]*	C_0	1.777 (1.275, 2.279)	2.151 (1.906, 2.397)	2.108 (1.861, 2.356)	1.894 (1.726, 2.063)
	D	0.472 (0.302, 0.641)	0.454 (0.326, 0.582)	0.590 (0.502, 0.679)	0.603 (0.490, 0.716)
	p	−1.078 (−1.629, 0.527)	−2.232 (−3.755, −0.708)	−1.324 (−1.904, −0.744)	−2.245 (−3.460, −1.030)
No. of molecules bound [$N(c)$]	M	175.3 (121.5, 229.1)	248.1 (158.1, 338.1)	144.4 (119.1, 169.6)	492.5 (393.5, 591.6)
$\sqrt{N(c)} = \sqrt{\dfrac{M \times c}{10^z + c}}$ [S2]	z	2.514 (2.178, 2.849)	2.525 (2.162, 2.887)	1.959 (1.731, 2.187)	1.843 (1.576, 2.111)
	t_0	1.660 (1.546, 1.773)	1.704 (1.531, 1.877)	1.421 (1.318, 1.524)	1.466 (1.416, 1.515)
Time to hemifusion [$t(c)$]	B	0.339 (0.207, 0.470)	0.433 (0.212, 0.655)	0.326 (0.184, 0.468)	0.414 (0.353, 0.478)
$t(c) = t_0 + \dfrac{B \times c}{10^{C_1} + c}$ [S3]†	C_1	1.461 (0.861, 2.060)	1.937 (0.985, 2.889)	1.982 (1.229, 2.736)	1.657 (1.415, 1.898)

Values in parenthesis represent 95% confidence bounds (lower, upper). For stabilization of all models, the hemifusion data without IgG were placed at an infinite low IgG concentration. All statistical analysis for fitting was performed using proc NLMIXED (SAS Version 9.2). Where necessary (Eq. **S1**), fitting involved a restriction that the lower asymptote was ≥ 0. Standard errors and 95% confidence limits were estimated using the delta method (1, 2). Eq. **S1**: E represents the proportion fusion events over total events, D and A represent respectively the upper and lower asymptote, p represents a slope factor, C represents the IgG/Fab concentration (in nanomolars) and C_0 represents the inflection point. Eq. **S2**: N represents the number of bound IgG/Fab defined as (median intensity)/(labeling correction × intensity per molecule), C is the concentration of IgG/Fab (in nanomolars), M is the maximum number of IgG/Fab that can bind and Z is the IgG/Fab concentration where the half-maximum number of molecules bind. Eq. **S3**: t represents the time to hemifusion, t_0 the time to hemifusion without IgG/Fab, B the interval between t_0 and the upper asymptote, C represents the IgG/Fab concentration (in nanomolars) and C_1 represents the IgG/Fab concentration corresponding to the geometric mean of t_0 and B being modeled on a $\log_{10}$ scale.

*Confidence intervals for 50% hemifusion efficiency reduction reported in Table 1 and *Results* were calculated using the delta method (1, 2) and the lowest degrees of freedom from the two models.

†Parameters B, C_1, and t_0 were modeled on a $\log_{10}$ scale.

1. Billingsley P (1986) *Probability and Measure* (John Wiley & Sons, Inc., New York).
2. Cox C (1998) *Encyclopedia of Biostatistics*, eds Armitage P, Colton T (John Wiley, New York), pp 1125–1127.

Movie S1. Complete virus disintegration. Full virus disintegration allowing outward diffusion of all HA–CR8020 complexes into the DSPE–PEG-supported bilayer shortly after full fusion. Labeling of the viral lumen by SRB was sufficient in this virus to allow visualization of the SRB molecules as they diffuse in the space between the glass coverslip and the tethered bilayer after full fusion. SRB fluorescence from the viral lumen is colored in magenta, CR8020 fluorescence is colored in green, overlap between the two is seen as white. (Scale bars, 2 μm.) The full fusion event is indicated with a magenta arrow and HA–CR8020 diffusion is indicated by green arrows.

Movie S1
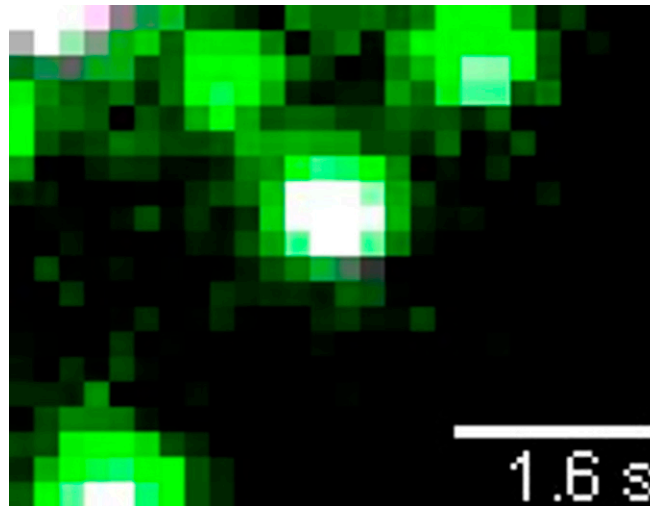
Movie S2. Partial virus disintegration. Partial virus disintegration allowing a portion of the HA–CR8020 complexes to diffuse outward into the DSPE–PEG-supported bilayer shortly after full fusion. The portion of HA–CR8020 observed to break off from the main virus particle is seen to itself disintegrate, with smaller HA–CR8020 clusters diffusing outward. SRB fluorescence from the viral lumen is colored in magenta, CR8020 fluorescence is colored in green, overlap between the two is seen as white. (Scale bars, 2 μm.) The full fusion event is indicated with a magenta arrow and the main HA–CR8020 diffusion event is indicated by green arrows.

Movie S2
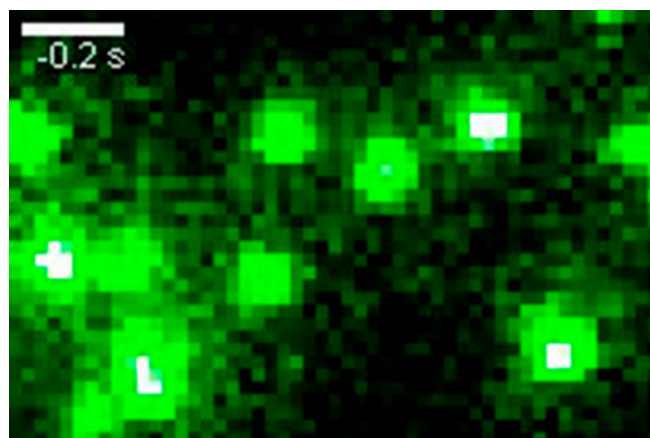
Movie S3. Long diffusion of small HA-CR8020 cluster. Release of a small cluster of HA–CR8020 complexes into the DSPE–PEG-supported bilayer after full fusion occurs. The cluster stays together for a substantial amount of time and undergoes long-range, 2D diffusion. SRB fluorescence from the viral lumen is colored in magenta, CR8020 fluorescence is colored in green, overlap between the two is seen as white. (Scale bars, 2 μm.) The full fusion event is indicated with a magenta arrow and the initial portion of the HA–CR8020 diffusion trajectory is indicated by green arrows.

Movie S3